Lignin-based chemical looping fuel cell using Ca2Fe2O5 as oxygen carrier for power generation

Atsuhiro Sumiya
Nagoya University
Naohiro Ikeda
Nagoya University
takashi hibino
hibino@urban.env.nagoya-u.ac.jp

Nagoya University

Article

Keywords:

Posted Date: December 5th, 2025

DOI: https://doi.org/10.21203/rs.3.rs-8225310/v1

Additional Declarations: No competing interests reported.

Lignin-based chemical looping fuel cell using $Ca_2Fe_2O_5$ as oxygen carrier for power generation

Atsuhiro Sumiya,[a] Naohiro Ikeda,[a] & Takashi Hibino [a,b]*

[a] Graduate School of Environmental Studies, Nagoya University, Nagoya 464-8601, Japan

[b] Department of Research, Nagoya Industrial Science Research Institute, Nagoya 460-0008, Japan

ABSTRACT

Recent research has developed systems for the chemical looping (CL) gasification of biomass using iron (Fe)-based metal oxides as oxygen carriers (OCs). The present study constructed a CL fuel cell utilizing lignosulfonate, a type of technical lignin, as the fuel and compared the performance obtained with $Ca_2Fe_2O_5$ and Fe_2O_3 as the OC materials. At 800 °C, the redox reactions of $Ca_2Fe_2O_5$ and Fe_2O_3 were found to be continuous and stepwise, respectively, during both chemical and electrochemical processes. This difference affected the reoxidation to regenerate the metal oxides upon discharge rather than the reduction to metallic Fe by the lignosulfonate. The $Ca_2Fe_2O_5$ was almost completely regenerated to its original structure whereas the Fe_2O_3 was only reoxidized to FeO and Fe_3O_4. The power densities of these fuel cells

were comparable, with values of 0.353 W cm^{-2} for the $Ca_2Fe_2O_5$ cell and 0.364 W cm^{-2} for the Fe_2O_3 cell. This equivalent performance is attributed to the similar internal resistances of both cells resulting from the strong effect of metallic Fe. However, the difference in reoxidation between the two OCs significantly affected the energy density. The $Ca_2Fe_2O_5$ cell showed an energy density of 0.755 Wh g^{-1} whereas a value of just 0.491 Wh g^{-1} was obtained from the Fe_2O_3 cell. Similar results were observed in trials with *Miscanthus sinensis*, a grassy biomass, as the fuel. The use of $Ca_2Fe_2O_5$ as the OC evidently increases the power generation efficiency of biomass-based fuel cells.

Introduction

The recycling of previously unused biomass such as technical lignin and grass clippings has attracted significant attention [1–4]. Although biomass valorization has been widely studied, improvements in production efficiency are required prior to practical applications [5–7]. Specifically, in the case that unused biomass is employed as a fuel for gasification power generation, conventional technologies have been unable to increase fuel utilization due to the effects of residual tar and char derived from lignin [8–10]. Consequently, the associated energy conversion efficiencies remains in the range of 20–30% [11]. Lignin has also been considered as a fuel for redox flow fuel cells, but the resulting power density and energy density values remain insufficient compared with those obtainable from conventional biomass power generation [12–14]. Additionally, this type of fuel cell requires an external dissolution process for the lignin.

Recent work has demonstrated chemical looping (CL) gasification based on employing unused biomass as a fuel [15–17]. CL is a technology in which a metal oxide (MO_x) serving as an oxygen carrier (OC) is converted to the corresponding metal (M) using a fuel, after which this metal is re-oxidized using water vapor (H_2O) or carbon dioxide (CO_2) to synthesize high-purity hydrogen (H_2) or carbon monoxide (CO). This technology has also been applied to iron (Fe)-air batteries, in which the reduction process uses H_2 produced in a solid oxide electrolysis cell (SOEC) while the oxidation process uses H_2O produced in a solid oxide fuel cell (SOFC) [18–20]. The authors recently reported an SOFC capable of directly using biomass. This device was operated using sodium lignosulfonate, a type of technical lignin, as a model biomass fuel, together with Fe_2O_3 as the OC [21]. The lignosulfonate was pyrolyzed and gasified in this cell at an operating temperature

of 800 °C and the gaseous reducing products gradually reduced the Fe_2O_3 to Fe. The overall reduction process is summarized by Eq. (1).

$$\text{lignosulfonate} + Fe_2O_3 \rightarrow 2Fe + \text{lignosulfonate residue} + xH_2 + yCO \quad (1)$$

The oxidation process in this cell proceeded through a combination of the following reactions.

$$nFe + mO^{2-} \rightarrow Fe_nO_m + 2me^- \quad (2)$$

$$xH_2 + 1/2xO^{2-} \rightarrow xH_2O + xe^- \quad (3)$$

$$yCO + 1/2yO^{2-} \rightarrow yCO_2 + ye^- \quad (4)$$

$$nFe + mH_2O \rightarrow Fe_nO_m + mH_2 \quad (5)$$

$$nFe + mCO_2 \rightarrow Fe_nO_m + mCO \quad (6)$$

It should be noted that the redox reactions in equations (1) to (6) continued as long as carbonaceous residue remained available during the discharge process. This fuel cell demonstrated a maximum power density of 0.364 W cm^{-2} and an energy density of 0.491 Wh g^{-1} [1]. However, assuming a higher heating value (HHV) of 2.68 Wh g^{-1} for the lignosulfonate [22], the power generation efficiency calculated from the energy density was just 18.3%. This low value was attributed to the generation of Fe_3C in addition to Fe during the reduction process and to the formation of only FeO (Fe^{2+}) and Fe_3O_4 (Fe^{2+}, Fe^{3+}) during the regenerative oxidation process. The latter effect caused the decrease in the ability of Fe_2O_3 as the OC [15,23–25].

The present study focused on the use of $Ca_2Fe_2O_5$ as an OC for power generation. This material has a brownmillerite structure and contains numerous oxygen ion vacancies within its crystal lattice. H_2 [24], CO [26], hydrocarbons [27] and biomass [28,29] have all been considered as fuels for the CL reduction process. $Ca_2Fe_2O_5$ was found to generate more H_2 and CO than Fe_2O_3 during the CL oxidation process and, unlike Fe_2O_3, reverted to its original structure following reoxidation. These differences between the two compounds can be explained by the Gibbs free energy change for the reoxidation reaction for each OC. Specifically, the processes $2Fe + 2CaO + H_2O$ or $CO_2 \rightleftharpoons Ca_2Fe_2O_5 + H_2$ (–41.4 kJ mol^{-1}) or CO (–40.8 kJ mol^{-1}) at 800 °C can be contrasted with $2Fe_3O_4 + H_2O$ or $CO_2 \rightleftharpoons 3Fe_2O_3 + H_2$ (+101.1 kJ mol^{-1}) or CO (+100.7 kJ mol^{-1}) at 800 °C. The main objective of this study was to assess the use of lignosulfonate as the fuel in the fuel cell. Another goal was to elucidate several aspects of this system. Firstly, to determine if the OC could be reduced to metallic Fe without producing Fe_3C in the reduction process. Secondly, to assess whether the anode reaction $2Fe + 2CaO + 3O^{2-} \rightarrow Ca_2Fe_2O_5 + 6e^-$ occurred during the oxidation process. Thirdly, to determine if the OC could be reoxidized to its original structure without undergoing carbonation to CaO, and lastly to evaluate any increases in power generation as a result of these factors. In addition to these items, the use of grassy biomass in place of lignosulfonate was investigated as a means of expanding the versatility of the technology.

Results and Discussion

Redox Properties of $Ca_2Fe_2O_5$ and Fe_2O_3

The redox properties of the $Ca_2Fe_2O_5$ and Fe_2O_3 powders were evaluated using temperature-programmed reduction (TPR) followed by temperature-programmed oxidation (TPO). **Figure 1a**

shows the H_2 consumption rates for the two samples when heated from 50 to 800 °C at a rate of 6.6 °C min^{-1} in a 2% H_2 (balance: helium (He)) flow. The TPR profile for the Fe_2O_3 exhibits a minor peak at approximately 250 °C and a major peak at approximately 460 °C, as well as a significant increase in hydrogen consumption between 550 and 800 °C. Gao et al. reported a similar TPR profile for Fe_2O_3, attributing the first peak to the $Fe_2O_3 \rightarrow Fe_3O_4$ transformation, the second peak to the $Fe_3O_4 \rightarrow FeO$ transformation, and the final hydrogen consumption stage to the reduction of FeO to Fe [30]. In contrast, the TPR profile for the $Ca_2Fe_2O_5$ in **Fig. 1a** contains a single peak at approximately 650 °C, consistent with results reported by Sun et al. [29] and Cai et al. [31]. **Figure 1b** shows the O_2 consumption rates for the two reduced samples when heated from 50 to 800 °C at 6.6 °C min^{-1} in a 2% O_2 (balance He) flow. The TPO profile for the Fe_2O_3 exhibits a feature that can be interpreted as either two steps or a broad peak between approximately 200 and 600 °C, while the TPO profile for the $Ca_2Fe_2O_5$ shows a single peak, similar to the TPR profile.

Several different models have been proposed for the reduction of metal oxides to metals, depending on particle size. Larger particles undergo reduction via a topochemical reaction mode, whereas smaller particles undergo uniform internal reduction according to a nucleation and growth model [32]. Although the reduction mechanism for $Ca_2Fe_2O_5$ has not yet been established, the appearance of a single peak in each of the TPO and TPR plots suggests a topochemical model in conjunction with structure-preserving reduction for this material.

In a previous study by the authors [21], Fe_2O_3 powder was used as a working electrode in a three-electrode cell (**Fig. S1b**) and was electrochemically oxidized and reduced at 800 °C by cyclic voltammetry. Three reduction peaks were observed during the reduction sweep (**Fig. 1c**) that were assigned to the following processes [33].

$$3Fe_2O_3 + 2e^- \rightleftarrows 2Fe_3O_4 + O^{2-} \qquad -0.45\ V\ (vs.\ O_2/O^{2-}) \qquad (7)$$

$$Fe_3O_4 + 2e- \rightleftarrows 3FeO + O^{2-} \qquad -0.96\ V\ (vs.\ O_2/O^{2-}) \qquad (8)$$

$$FeO + 2e^- \rightleftarrows Fe + O^{2-} \qquad -1.07\ V\ (vs.\ O_2/O^{2-}) \qquad (9)$$

When the electrode was swept in the oxidation direction, a broad oxidation peak appeared at −0.76 V together with a less intense oxidation peak at −0.23 V. These results are consistent with those obtained for TPR and TPO in the present work and indicate that the series of redox reactions transforming Fe_2O_3 into Fe can be promoted by chemical and electrochemical systems. In contrast, when $Ca_2Fe_2O_5$ was used as the working electrode, no redox peaks were observed under the same conditions. Hence, at 800 °C, it appears that $Ca_2Fe_2O_5$ is electrochemically reduced and re-oxidized in a manner similar to Fe_2O_3 although, in contrast, these redox reactions occur sequentially.

To obtain a better understanding of the redox properties of the $Ca_2Fe_2O_5$ and Fe_2O_3 samples, each powder was placed in the anode chamber of a gas flow cell (**Fig. S1c**) and heated to 800 °C. Argon (Ar), H_2 and Ar flows were then sequentially and continuously supplied to the anode chamber. **Figure 2a** plots the open-circuit voltage (OCV) data recorded during these trials. It is apparent that the OCV increased upon switching to H_2 but this increase occurred in a stepwise

manner in the trial using the Fe_2O_3 and in a single step with the $Ca_2Fe_2O_5$. This difference is consistent with the trends observed in the TPR and CV data. The subsequent switch back to Ar reduced both OCV values to approximately 0.9 V due to the effect of O_2 present as an impurity in the Ar flow.

After 500 sec, a constant current of 0.1 A cm^{-1} was applied to each cell while maintaining the Ar flow. As shown in **Fig. 2b**, both cells were successfully discharged, reaching short-circuit times of 1136 sec for $Ca_2Fe_2O_5$ and 963 sec for Fe_2O_3. Interestingly, the X-ray diffraction (XRD) patterns acquired from the discharged samples showed peaks attributable to $Ca_2Fe_2O_5$ and additional peaks associated with $CaFe_2O_4$ for the former (**Fig. 2c**) and peaks attributable to Fe_2O_3 along with additional peaks related to FeO and Fe_3O_4 for the latter (**Fig. 2d**). These results indicate that the reduced Fe species in both samples was re-oxidized to essentially the original oxides via the anode reaction. Ishihara et al. reported that, at 800 °C and a cell voltage of 0.9 V, either FeO or Fe_3O_4 is generated [18]. Assuming that the reduced Fe species before discharge was Fe_3O_4 in the present case, the anode reaction would have been as follows.

$$Fe_3O_4 + 3CaO + 0.5O^{2-} \rightarrow 1.5Ca_2Fe_2O_5 + e^- \quad (10)$$

Based on the discharge charge in **Fig. 2b**, it was calculated that the quantity of reoxidized Fe_3O_4 was 1.69 mmol as the metal equivalent. Assuming that the Fe species was FeO, 0.57 mmol would have been generated. The number of moles of $Ca_2Fe_2O_5$ added to the cell was 1.26 mmol as the metal equivalent, which was close to the average of the values above. Thus, it appears that almost all the Fe species assumed to have been produced were reoxidized by discharging the cell.

Combustion and Pyrolysis Characteristics of Lignosulfonate and its Reaction with Metal Oxides

The composition of the lignosulfonate used in this study was 41.6% C, 33.1% O, 16.1% Na and 5.8% S [34]. This carbon content is close to the 40% reported by Mei et al. [22]. The combustion and pyrolysis characteristics of the lignosulfonate were assessed using thermogravimetry and differential thermal analysis (TG–DTA). In these trials, a sample was heated to approximately 500 °C to induce combustion in an air flow, and also pyrolyzed more gradually by heating from approximately 400 to 800 °C in an Ar flow (**Fig. S2**). The residual mass following pyrolysis up to 800 °C was found to be greater than that after combustion. The pyrolysis residue was also assessed using Raman spectroscopy. While no clear peaks were obtained from the material prior to pyrolysis, following pyrolysis peaks were observed at 1320 and 1600 cm^{-1}. These were attributed to the presence of amorphous carbon (referred to here as the D band) and graphite (the G band), respectively (**Fig. S3**). These results demonstrate that graphite and amorphous carbon remained in the sample after pyrolysis at 800 °C.

In subsequent experiments, a quantity of $Ca_2Fe_2O_5$ or Fe_2O_3 (equivalent to 1.26 mmol of the metal) was mixed with 0.25 g of lignosulfonate and heated from room temperature to 800 °C at a rate of 6.6 °C min^{-1} in a He flow. **Figure 3** shows the concentrations of gaseous effluent components produced from the mixtures, along with data for the lignosulfonate alone for comparison. In all cases, CO_2 was produced beginning at approximately 200 °C, CH_4 was obtained from approximately 300 °C, and CO and H_2 were observed starting at approximately

600 °C. $Ca_2Fe_2O_5$ exhibited a more pronounced effect on the reaction with lignosulfonate than Fe_2O_3. In particular, CO_2 and CO were consistently produced in greater amounts using the former material. Furthermore, above 750 °C, the decrease in CO_2 concentration and the increase in CO concentration were more significant. The lignosulfonate/$Ca_2Fe_2O_5$ mixture was evidently more susceptible to combustion and subsequent gasification via the Boudouard reaction [35], shown in Eq. 11, compared with the lignosulfonate/Fe_2O_3 combination.

$$C + CO_2 \rightarrow 2CO \quad (11)$$

Comparative Performance of SOFCs Using $Ca_2Fe_2O_5$ and Fe_2O_3 as OCs

A mixture of 0.25 g of lignosulfonate and $Ca_2Fe_2O_5$ or Fe_2O_3 (each 1.26 mmol as the metal equivalent) was transferred into the anode chamber of a batch cell (**Fig. S1d**) and heated to 800 °C at a rate of 6.6 °C min^{-1}. **Figure 4a** shows the current density–voltage (*I–V*) and current density–power density (*I–P*) curves obtained from the two SOFCs. The OCV values for both cells were approximately 1 V and the slopes of the *I–V* curves were similar. This similarity was also confirmed by acquiring the impedance spectra of both cells under OCV conditions (**Fig. S4**). Maximum power densities of 0.353 and 0.364 W cm^{-2} were obtained from the $Ca_2Fe_2O_5$ and Fe_2O_3 cell, respectively. These values exceed those reported for lignin-fueled redox flow fuel cells (as an example, 0.269 W cm^{-2} [13]) as a consequence of the differences in the *I–V* slopes, meaning the internal resistance, of the present cells and those evaluated in prior work. It should be noted that an inflection point appears at approximately 0.6 V in the *I–V* curves for both cells in **Fig. 4a**, likely due to the oxidation of nickel (Ni), an anode component, during cell discharge [36].

Figure 4b presents the voltages obtained from the $Ca_2Fe_2O_5$ and Fe_2O_3 cells over time in conjunction with a current density of 0.1 A cm^{-2}. In both cases, the initial voltage remained at approximately 0.9 V for up to 6000 s. This voltage plateau is attributed to the action of the lignosulfonate as a reducing agent, because this phenomenon was not observed in the absence of lignosulfonate (see **Fig. 2b**). The voltage provided by the Fe_2O_3 cell was found to rapidly decrease after this plateau, with a short circuit occurring at 8020 sec. In contrast, the $Ca_2Fe_2O_5$ cell exhibited a voltage plateau that was extended by approximately 2000 s. The energy density per gram of the lignosulfonate was calculated by integrating the voltage–time (*V–time*) curve and multiplying this value by the discharge current of 0.05 A. The resulting values were 0.458 Wh g^{-1} for the $Ca_2Fe_2O_5$ cell and 0.365 Wh g^{-1} for the Fe_2O_3 cell, as expected. Note that, hereafter, the term gravimetric energy density is used to refer to the energy density per gram of lignosulfonate. It is also noteworthy that the enhanced performance provided by the $Ca_2Fe_2O_5$ was observed not only in trials with lignosulfonate but also when using *Miscanthus sinensis*, a type of grassy biomass, as the fuel (**Fig. S5**). This biomass consisted of 37.5% cellulose, 22.9% hemicellulose, 14.9% lignin, 9.5% ash and other materials [37]. It is thus reasonable to conclude that cellulose and hemicellulose could also be used as fuels for these OCs.

The performance of $Ca_2Fe_2O_5$ as the OC can also be understood by comparing this material with a mixture of CaO and Fe_2O_3 and with $CaFe_2O_4$. Specifically, the gravimetric energy density for these specimens decreased in the order of $Ca_2Fe_2O_5$ > $CaFe_2O_4$ = CaO + Fe_2O_3 > Fe_2O_3 (**Fig. S6**). A similar performance hierarchy between $Ca_2Fe_2O_5$ and $CaFe_2O_4$ has also been observed in

trials involving the CL gasification of biomass [29,38] and is attributed to the ability of $CaFe_2O_4$ to undergo more than two reduction steps [38]. It has also been demonstrated that a $CaO + Fe_2O_3$ mixture generates both $Ca_2Fe_2O_5$ and $CaFe_2O_4$ during reoxidation [39].

XRD analyses were performed to investigate the reduction of $Ca_2Fe_2O_5$ and Fe_2O_3 by biomass and to also assess the reoxidation of these compounds upon discharge. **Figures 5a and 5b** show XRD patterns for these two samples, respectively, before and after discharge. These data demonstrate that both samples were reduced to metallic Fe at the OCV, although Fe_3C was also generated in the case of the Fe_2O_3 cell. Following discharge, the OC in the $Ca_2Fe_2O_5$ cell returned almost entirely to its original structure, whereas the OC in the Fe_2O_3 cell was only regenerated to FeO and Fe_3O_4. This latter result differs from that in **Fig. 2d**, in which regeneration to Fe_2O_3 is apparent. Interestingly, Strazzolini et al. [25] reported that Fe_3C formed during reduction by biomass may prevent reoxidation to Fe_2O_3. The overall reoxidation process during discharge in the present work is assumed to proceed as follows.

$$2Fe + 2CaO + 3O^{2-} \rightarrow Ca_2Fe_2O_5 + 6e^- \quad (11)$$

Based on this equation, it was calculated that 1.68 mmol of Fe was reoxidized, which exceeds the original quantity of $Ca_2Fe_2O_5$ (1.26 mmol). This outcome suggests that either the unused carbonaceous residue functioned as a new reducing agent during discharge or the CO generated from the residue via the Boudouard reaction participated in the anode reaction. In any case, it appears that the excess unused fuel contributed to the subsequent discharge.

From the results discussed above, it appears that an excess of biomass relative to the amount of the OC effectively promotes the discharge process. Hence, subsequent trials investigated the relationship between the gravimetric energy density and the mass of the lignosulfonate. In these experiments, the amounts of $Ca_2Fe_2O_5$ and Fe_2O_3 were fixed at 1.26 mmol as the metal equivalents while the mass of the lignosulfonate was varied. **Figure 6a** shows the change in cell voltage over time when discharging at a constant current of 0.1 A cm^{-2} using $Ca_2Fe_2O_5$ as the OC. A minimal voltage plateau was observed at a mass of 0.15 g and the cell voltage at each point in time was found to increase with increasing lignosulfonate mass. Similar results were observed in the cell using Fe_2O_3 as the OC (**Fig. S7**). These data indicate that the additional lignosulfonate was effectively utilized as either a reducing agent or a fuel.

Gravimetric energy densities were calculated based on the data in **Fig. 6a** and **Fig. S7** and are plotted against the mass of lignosulfonate in **Fig. 6b**. Although the gravimetric energy density should essentially be independent of the fuel mass, the calculated values tended to increase along with the fuel mass in both the $Ca_2Fe_2O_5$ and Fe_2O_3 cells. However, the gravimetric energy density for the $Ca_2Fe_2O_5$ cell remained constant at masses above 0.5 g whereas that for the Fe_2O_3 cell decreased at 0.5 g. It is noteworthy that the incorporation of $Ca_2Fe_2O_5$ produced a maximum gravimetric energy density of 0.755 Wh g^{-1}. This value corresponds to 28.2% of the HHV of 2.68 Wh g^{-1} [22] for lignosulfonate and exceeds the value of 18.3% obtained from the Fe_2O_3 cell. Note that these percentages will vary depending on the HHV value that is selected.

XRD patterns were obtained from the OCs following discharge to further assess the effect of fuel mass on the gravimetric energy density. **Figures 6c and 6d** present the patterns associated with the use of $Ca_2Fe_2O_5$ and Fe_2O_3 as the OC, respectively. Regardless of the mass, peaks attributed to $Ca_2Fe_2O_5$ can be seen in the patterns generated after discharge as shown in Figure 6(c), while peaks attributed to FeO and Fe_3O_4 are evident in **Fig. 6d**. A notable feature of these data is that the effect of fuel mass on the peak attributed to metallic Fe differed between the $Ca_2Fe_2O_5$ and Fe_2O_3 cells. Specifically, the metallic Fe peak became more intense with lower mass in the former but with higher mass in the latter.

Matsui et al. reported that the Ni in Ni-based anodes is readily oxidized at high fuel utilization [40]. Based on this, a relationship between the lignosulfonate amount and the discharge characteristics of the $Ca_2Fe_2O_5$ can be proposed. In this mechanism, a low fuel supply produces little residue during discharge such that Ni oxidation occurs before the anode reaction is complete and the discharge cannot be sustained. As a result, metallic Fe remains even after discharge, lowering the energy density. If the fuel supply is increased, the residue allows Fe reoxidation to be completed before the Ni is oxidized, resulting in a high energy density. In contrast, in the case of the Fe_2O_3 cell, a greater fuel supply is thought to promote the formation of Fe_3C or the growth of Fe particles [41], suppressing the reoxidation of metallic Fe. Unlike conventional CL gasification, the present fuel cell appears to comprise a complex circulating system of carbonaceous residues, metallic Fe and Ni, $Ca_2Fe_2O_5$ or Fe_2O_3, oxide ions and electrons during the discharge oxidation process. Even so, in terms of both the CL gasification process and the fuel cell, $Ca_2Fe_2O_5$ is a better OC than Fe_2O_3.

Conclusions

This study investigated the performance of $Ca_2Fe_2O_5$ and Fe_2O_3 as OC materials in lignosulfonate-fueled CL fuel cells. The chemical and electrochemical redox processes for these materials were consistent. $Ca_2Fe_2O_5$, unlike Fe_2O_3, was found to undergo continuous redox reactions and almost complete regeneration to its original structure. This difference had a greater impact on the energy density than on the power density of the cell. A cell incorporating $Ca_2Fe_2O_5$ as the OC exhibited a gravimetric energy density of 0.755 Wh g^{-1}, which was higher than the value of 0.491 Wh g^{-1} obtained using Fe_2O_3 as the OC. Notably, a similar difference in energy density between the OC materials was seen when using a grassy biomass as the fuel. These results clearly demonstrate that the power generation efficiency of the present biomass-based fuel cell was improved when utilizing $Ca_2Fe_2O_5$ as the OC for the CL system.

Experimental Section

Materials

$Ca_2Fe_2O_5$ and Fe_2O_3 were employed as OCs in this study. The preparation of the former has been described in detail elsewhere [42]. In brief, the required amounts of CaO (Wako Chemical) and Fe_2O_3 (Wako Chemical) were mixed, pressed into a pellet, and then calcined in air at 1000 °C for 3 h. The resulting $Ca_2Fe_2O_5$ was then ground with a mortar and pestle. The Fe_2O_3 was used as received without further treatment. Sodium lignosulfonate (Tokyo Chemical Industry) was used

as the lignin sample. The *Miscanthus sinensis* employed as the biomass was collected at sites around the Nagoya University campus.

SOFC fabrication

The cell used in this study consisted of a NiO–4 mol% yttria-stabilized zirconia (4YSZ) diffusion layer (thickness ~500 μm), a NiO–8 mol% YSZ (8YSZ) reaction layer (thickness ~30 μm), an 8YSZ layer (thickness ~5 μm), a $Ce_{0.9}Gd_{0.1}O_{1.95}$ (GDC) layer (thickness ~5 μm), a $La_{0.6}Sr_{0.4}CoO_3$ (LSC) + GDC protective layer (thickness ~70 μm) and an LSC layer (thickness ~30 μm) (Figure S1). The cell was fabricated by tape casting using a previously reported procedure.[21] The anode diffusion and reaction layers were prepared by combining NiO and 4YSZ powders and NiO and 8YSZ powders, respectively, in a volume ratio of 1:1, after which spherical acrylic beads with a particle size of 1.5 μm were added at a concentration of 20 vol% as a pore agent for the diffusion layer. The slurries for the anode and electrolyte tapes were prepared by mixing the corresponding powdered components with suitable quantities of 1-butanol and isopentyl acetate (as solvents), dibutyl phthalate (as a plasticizer) and propylene glycol ether derivative (as a dispersant) in a ball mill, after which polyvinyl butyral resin was added to prepare a uniform suspension. Each suspension was then cast onto polyethylene terephthalate (PET) foil using a doctor blade. The tapes peeled off from the foil were laminated in the order of diffusion layer, reaction layer, electrolyte membrane and protective membrane, pressed at 90 °C and 1 MPa for 10 s, degreased at 500 °C for 2 h, and finally sintered at 1325 °C for 5 h. The LSC cathode (area 0.5 cm^2) was printed on the surface of the protective membrane and sintered at 950 °C for 5 h. The porosity of the anode diffusion layer was 24.0%.

Characterization

TG–DTA data were obtained using a Shimadzu DTG-60 instrument while heating specimens from room temperature to 800 °C at a heating rate of 6.6 °C min^{-1} in an air or Ar flow. XRD patterns were collected over the 2θ range of 20–80° using a Rigaku MiniFlex II diffractometer equipped with a monochromator and a Cu Kα radiation source (1.5432 Å). The peak assignments were made using the International Centre for Diffraction Data database. Raman spectra were obtained with a Jasco NRS-1000 incorporating a 3.5 mW laser operating at 532 nm. TPR, TPO and catalytic reactions were conducted by packing the sample into an alumina boat that was subsequently transferred into a quartz tube. The boat was heated from room temperature to 800 °C at a rate of 6.6 °C min^{-1} in a He flow. The effluent gas was sampled online at 50 or 100 °C intervals and sent to a gas chromatograph (Varian CP-4900). H_2, O_2, CH_4 and CO were separated using a molecular sieve column held at 100 °C while CO_2 was separated using a Porapak Q column at 80 °C. Scanning electron microscopy (SEM) images were acquired using a Keyence VE-8800 at an accelerating voltage of 2 kV.

Electrochemical measurements

Three-electrode, gas flow and batch cells were utilized in this work. The three-electrode cell was prepared by applying a $Ca_2Fe_2O_5$ or Fe_2O_3 aqueous slurry and a platinum (Pt) paste (Tanaka Kikinzoku TK7605) to the upper and lower surfaces, respectively, of a 1-mm-thick 8YSZ disk (Tosoh TZ-8Y) in a circular pattern with an area of 0.5 cm^2. A Pt reference electrode was attached to the side of the disk to measure the anode potential during CV trials. All the cells were set up by placing the cell assembly between two alumina tube systems. A tube closed at one end was used for the anode chamber in the batch cell while the other two cells used double tubes. In each case, the double tubes comprised the cathode chamber. A Pt mesh was used as the current collector for both electrodes. A glass ring gasket with a softening temperature of 720 °C was

used as the sealing material for the anode chamber. The anode chambers of the flow cell and batch cell were filled with $Ca_2Fe_2O_5$ or Fe_2O_3 powder and with a powdered mixture of each metal oxide and lignosulfonate, respectively. The mass of the fuel was in the range 0.15–0.75 g whereas the quantity of the metal oxide was fixed at 1.26 mmol as the metal equivalent. Schematic diagrams of the cell units constructed in this work are presented in Figure S1. The furnace temperature was controlled by a thermocouple and the unit was heated from room temperature to 800 °C at a rate of 6.6 °C min^{-1}. Ar and H_2 (Ar before H_2 and Ar after H_2) were supplied to the anodes of the three-electrode and the flow cells, respectively, at rates of 30 mL min^{-1}. All electrochemical measurements were performed using a potentiostat–galvanostat (Solartron 1287) and a frequency-response analyzer (Solartron 1260). CV profiles were recorded over the potential range from zero to +1.5 V at a scan rate of 50 mV sec^{-1}. The impedance spectra were collected at the OCV over the frequency range of 0.1–10^6 Hz. The *I–V* curves were recorded at a scan rate of 5 mV sec^{-1} while *V–time* data were acquired at a current density of 0.1 A cm^{-2}.

Data availability

The datasets generated and/or analyzed during the current study are available within the paper. Other materials and data are available from the corresponding author, Takashi Hibino, upon reasonable request.

References

1. Kumar, A. & Samadder, S. R. A review on technological options of waste to energy for effective management of municipal solid waste. *Waste Manag.* **69**, 407–422 (2017). 10.1016/j.wasman.2017.08.046.

2. Heidari, R., Yazdanparast, R. & Jabbarzadeh, A. Sustainable design of a municipal solid waste management system considering waste separators: A real-world application. *Sustain. Cities Soc.* **47**, 101457 (2019). 10.1016/j.scs.2019.101457

3. Al-Shetwi, A. Q. Sustainable development of renewable energy integrated power sector: Trends, environmental impacts, and recent challenges. *Sci. Total Environ.* **822**, 153645 (2022). 10.1016/j.scitotenv.2022.153645.

4. Inghels, D., Dullaert, W., Aghezzaf, E.-H. & Heijungs, R. Towards optimal trade-offs between material and energy recovery for green waste. *Waste Manage.* **93**, 100–111 (2019). 10.1016/j.wasman.2019.05.023

5. Alriols, M. G., García, A., Llano-Ponte, R. & Labidi, J. Combined organosolv and ultrafiltration lignocellulosic biorefinery process. *Chem. Eng. J.* **157**, 113–120 (2010). 10.1016/j.cej.2009.10.058

6. Sarika, P. R., Nancarrow, P., Khansaheb, A. & Ibrahim, T. Bio-based alternatives to phenol and formaldehyde for the production of resins. *Polymers* **12**, 2237 (2020). 10.3390/polym12102237

7. Caravaca, A., Garcia-Lorefice, W. E., Gil, S., de Lucas-Consuegra, A. & Vernoux, P. Towards a sustainable technology for H_2 production: direct lignin electrolysis in a continuous-flow polymer electrolyte membrane reactor. *Electrochem. Commun.* **100**, 43–47 (2019). 10.1016/j.elecom.2019.01.016

8. Sikarwar, V. S., Zhao, M., Clough, P., Yao, J., Zhong, X., Memon, M. Z., Shah, N., Anthony, E. J. & Fennell, P. S. An overview of advances in biomass gasification. *Energy Environ. Sci.* **9**, 2939–2977 (2016).

10.1039/C6EE00935B

9. Safarian, S., Unnþórsson, R. & Richter, C. A review of biomass gasification modelling. *Renew. Sust. Energy Rev.* **110**, 378–391 (2019).

10.1016/j.rser.2019.05.003

10. Cao, L., Yu, I. K. M., Xiong, X., Tsang, D. C. W., Zhang, S., Clark, J. H., Hu, C., Ng, Y. H., Shang, J. & Ok, Y. S. Biorenewable hydrogen production through biomass gasification: A review and future prospects. *Environmental Research.* **186**, 109547 (2020).

10.1016/j.envres.2020.109547

11. Jamil, F., Inayat, A., Hussain, M., Akhter, P., Abideen, Z., Ghenaï, C., Shanableh, A. & Abdellatief, T. M. Valorization of waste biomass to biofuels for power production and transportation in optimized way: A comprehensive review. *Adv. Energy Sustainability Res.* **5**, 2400104 (2024).

10.1002/aesr.202400104

12. Ouyang, D., Gao, D., Qiang, Y. & Zhao, X. Highly-efficient conversion of lignin to electricity by nickel foam anode loaded with solid electrocatalysts. *Appl. Catal. B Environ.* **328**, 122491 (2023).

10.1016/j.apcatb.2023.122491

13. Liang, T., Zu, X., Liu, B., Qiu, X., Xie, Z., Wang, X. & Yang, D. A low temperature and high-power density lignin flow fuel cell via an efficient CoMn-LDH electrocatalyst with superhydrophilic intercalation. *Green Chem.* **26**, 4811–4819 (2024).

10.1039/D4GC00476K

14. Danlu, Z., Peng, W., Qiqi, D., Yan, X., Qingyou, L., Xu, Z., Chuanfu, L. & Wu, L. Dual-functional lignin fuel cells: Coupling electricity generation with lignosulfonate valorization using dodecyl sulfate-intercalated NiS_2 anode catalysts. *Chem. Eng. J.* **504**, 158566 (2025).

10.1016/j.cej.2024.158566

15. Zhao, X., Zhou, H., Sikarwar, V. S., Zhao, M., Park, A.-H. A., Fennell, P. S., Shen, L. & Fan, L.-S. Biomass-based chemical looping technologies: the good, the bad and the future. *Energy Environ. Sci.* **10**, 1885–1910 (2017).

10.1039/C6EE03718F

16. Goel, A., Moghaddam, E. M., Liu, W., He, C. & Konttinen, J. Biomass chemical looping gasification for high-quality syngas: A critical review and technological outlooks. *Energ. Convers. Manage.* **268**, 116020 (2022).

10.1016/j.enconman.2022.116020

17. Raja, K., Packiyam, T., Saravanan, A., Yaashikaa, P. R. & Vickram, A. S. Assessing the techno-economic and sustainable potential of chemical looping for bioenergy production from organic solid wastes. *Energy Storage Sav.* **4**, 14–26 (2025).

10.1016/j.enss.2024.11.007

18. Inoishi, A., Ju, Y. W., Ida, S. & Ishihara, T. Fe–air rechargeable battery using oxide ion conducting electrolyte of Y_2O_3 stabilized ZrO_2. *J. Power Sources* **229**, 12–15 (2013).

10.1016/j.jpowsour.2012.11.121

19. Zhao, X., Xu, N., Li, X., Gong, Y. & Huang, K. Solid oxide iron-air rechargeable battery - a new energy storage mechanism. *ECS Trans.* **50**, 115–123 (2013).

10.1149/05045.0115ecst

20. Trocino, S., Lo Faro, M., Zignani, S. C., Antonucci, V. & Aricò, A. S. High performance solid-state iron-air rechargeable ceramic battery operating at intermediate temperatures (500–650 °C). *Appl. Energy* **233–234**, 386–394 (2019).

10.1016/j.apenergy.2018.10.022

21. Sumiya, A., Ikeda, N. & Hibino, T. High-power, high-energy solid oxide fuel cell using lignosulfonate as energy source and Fe_2O_3 as pseudo-fuel. *J. Mater. Sci.* **60**, 21310–21320 (2025).

10.1007/s10853-025-11631-w

22. Mei, C., Hu, C., Hu, Q., Sun, C., Li, L., Liang, X., Dong, Y. & Gu, X. Effective depolymerization of sodium lignosulfonate over SO_4^{2-}/TiO_2 catalyst. *Catalysts* **10**, 995 (2020).

10.3390/catal10090995

23. Kwong, K. Y., Harrison, A. R. P., Gebers, J. C., Dennis, J. S. & Marek, E. J. Chemical looping combustion of a biomass char in Fe_2O_3-, CuO-, and $SrFeO_{3-\delta}$-based oxygen carriers. *Energy Fuels* **36**, 9437–9449 (2022).

10.1021/acs.energyfuels.2c01269

24. Cai, Y., Wang, C., Zhong, M., Zhang, Z., Xiao, B., Xu, T. & Wang, X. Evaluation of redox activity of brownmillerite-structured $Ca_2Fe_2O_5$ oxygen carrier for chemical looping applications. *Int. J. Hydrog. Energy* **48**, 27112–27126 (2023).

10.1016/j.ijhydene.2023.03.395

25. Strazzolini, A., Basbus, J. F., de Leitenburg, C., Llorca, J., Boaro, M. & Trovarelli, A. Design of Ni-promoted $Ca_2Fe_2O_5$/modified ceria as oxygen carrier for fast and carbon-resistant chemical-looping steam methane reforming. *Appl. Catal. B-Environ.* **383**, 126037 (2026).

10.1016/j.apcatb.2025.126037

26. Chan, M. S. C., Liu, W., Ismail, M., Yang, Y., Scott, S. A. & Dennis, J. S. Improving hydrogen yields, and hydrogen: steam ratio in the chemical looping production of hydrogen using $Ca_2Fe_2O_5$. *Chem. Eng. J.* **296**, 406–411 (2016).

10.1016/j.cej.2016.03.132

27. Kosaka, T. & Otomo, J. Microstructural stabilization and redox reactions involving structural phase transformation of calcium ferrite oxygen carriers in chemical looping combustion. *ACS Appl. Eng. Mater.* **3**, 2, 401–409 (2025).

10.1021/acsaenm.4c00728

28. Sun, Z., Chen, S., Russell, C. K., Hu, J.; Rony, A. H., Tan, G., Chen, A., Duan, L., Boman, J., Tang, J., Chien, T., Fan, M. & Xiang, W. Improvement of H_2-rich gas production with tar abatement from pine wood conversion over bi-functional $Ca_2Fe_2O_5$ catalyst: Investigation of inner-looping redox reaction and promoting mechanisms. *Appl. Energy* **212**, 931–943 (2018).

10.1016/j.apenergy.2017.12.087

29. Sun, Z., Wu, X., Russell, C. K., Dyar, M. D., Sklute, E. C., Toan, S., Fan, M., Duan, L. & Xiang, W. Synergistic enhancement of chemical looping-based CO_2 splitting with biomass cascade utilization using cyclic stabilized $Ca_2Fe_2O_5$ aerogel. *J. Mater. Chem. A* **7**, 1216–1226 (2019).

10.1039/C8TA10277E

30. Gao, Z., Wu, D., Barakat, M., Sun, L., Gong, F. & Xiao, R. Improving the reactivity and stability of Fe_2O_3/Al_2O_3 in chemical looping process by optimizing the Al_2O_3 precursor. *Ind. Eng. Chem. Res.* **63**, 3092–3103 (2024).

10.1021/acs.iecr.3c04066

31. Cai, Y., Wang, C., Zhang, Z., Zhong, M., Wu, Q., Xiao, B., Xu, T. & Wang, X. Performance optimization of $Ca_2Fe_2O_5$ oxygen carrier by doping different metals for coproduction syngas and hydrogen with chemical looping gasification and water splitting. *J. Energy Inst.* **111**, 101391 (2023).

10.1016/j.joei.2023.101391

32. Tiernan, M. J., Barnes, P. A. & Parkes, G. M. B. Reduction of iron oxide catalysts: the investigation of kinetic parameters using rate perturbation and linear heating thermoanalytical techniques. *J. Phys. Chem. B* **105**, 220–228 (2001).

10.1021/jp003189+

33. Li, H., Jia, L., Liang, J.-l., Yan, H.-y., Cai, Z.-y. & Reddy, R. G. Study on the direct electrochemical reduction of Fe_2O_3 in NaCl–$CaCl_2$ melt. *Int. J. Electrochem. Sci.* **14**, 11267–11278 (2019).

10.20964/2019.12.68

34. Hibino, T., Kobayashi, K., Teranishi, S. & Hitomi, T. Solid oxide fuel cell using municipal solid waste directly as fuel: biomass, resin, plastic, and food waste. *ACS Sustainable Chem. Eng.* **9**, 3124–3136 (2021).

DOI: 10.1021/acssuschemeng.0c07657

35. Bakari, R., Kivevele, T., Huang, X. & Jande, Y. A. C. Catalytic supercritical water gasification of biomass waste using iron-doped alkaline earth catalysts. *Biomass Conv. Bioref.* **14**, 7487–7506 (2024).

10.1007/s13399-022-02800-x

36. Kawasaki, T., Matsuda, J., Tachikawa, Y., Lyth, S. M., Shiratori, Y., Taniguchi, S. & Sasaki, K. Oxidation-induced degradation and performance fluctuation of solid oxide fuel cell Ni anodes under simulated high fuel utilization conditions. *Int. J. Hydrogen Energy* **44**, 9386–9399 (2019).

10.1016/j.ijhydene.2019.02.136

37. Hibino, T., Kobayashi, K. & Hitomi, T. Biomass solid oxide fuel cell using solid weed waste as fuel. *Electrochim. Acta* **388**, 138681 (2021).

10.1016/j.electacta.2021.138681

38. Ismail, M., Liu, W., Chan, M. S. C., Dunstan, M. T. & Scott, S. A. Synthesis, application, and carbonation behavior of $Ca_2Fe_2O_5$ for chemical looping H_2 production. *Energy Fuels* **30**, 6220–6232 (2016).

10.1021/acs.energyfuels.6b00631

39. Ismail, M., Liu, W., Dunstan, M. T. & Scott, S. A. Development and performance of iron based oxygen carriers containing calcium ferrites for chemical looping combustion and production of hydrogen. *Int. J. Hydrogen Energy* **41**, 4073–4084 (2016).

10.1016/j.ijhydene.2015.11.066

40. Matsui, T., Kishida, R., Muroyama, H. & Eguchi, K. Comparative study on performance stability of Ni–oxide cermet anodes under humidified atmospheres in solid oxide fuel cells. *J. Electrochem. Soc.* **159**, F456–F460 (2012).

10.1149/2.053208jes

41. Liu, Y. H., Guan, Y., Lin, X. L., Wang, B. & Lyu, Q. Research progress and perspectives of solid fuels chemical looping reaction with Fe-based oxygen carriers. *Energy Fuels* **36**, 13956–13984 (2022).

10.1021/acs.energyfuels.2c02802

42. Hirabayashi, D., Yoshikawa, T., Mochizuki, K., Suzuki, K. & Sakai, Y. Formation of brownmillerite type calcium ferrite ($Ca_2Fe_2O_5$) and catalytic properties in propylene combustion. *Catal. Lett.* **110**, 155–160 (2006).

10.1007/s10562-006-0104-0

Author information

Authors and Affiliations

Graduate School of Environmental Studies, Nagoya University, Nagoya 464-8601, Japan

Atsuhiro Sumiya, Naohiro Ikeda & Takashi Hibino

Department of Research, Nagoya Industrial Science Research Institute, Nagoya 460-0008, Japan

Takashi Hibino

Contributions

A.S., N.I. and T.H. contributed equally. N.I. conducted all experiments. A.S. contributed to the preparation of SOFCs. T.H. wrote the manuscript.

Corresponding author: Takashi Hibino

E-mail: hibino@urban.env.nagoya-u.ac.jp

Ethics declarations

Competing interests

The authors declare no competing financial interest.

Supplementary information

Below is the link to the electronic supplementary material.

Supplementary information

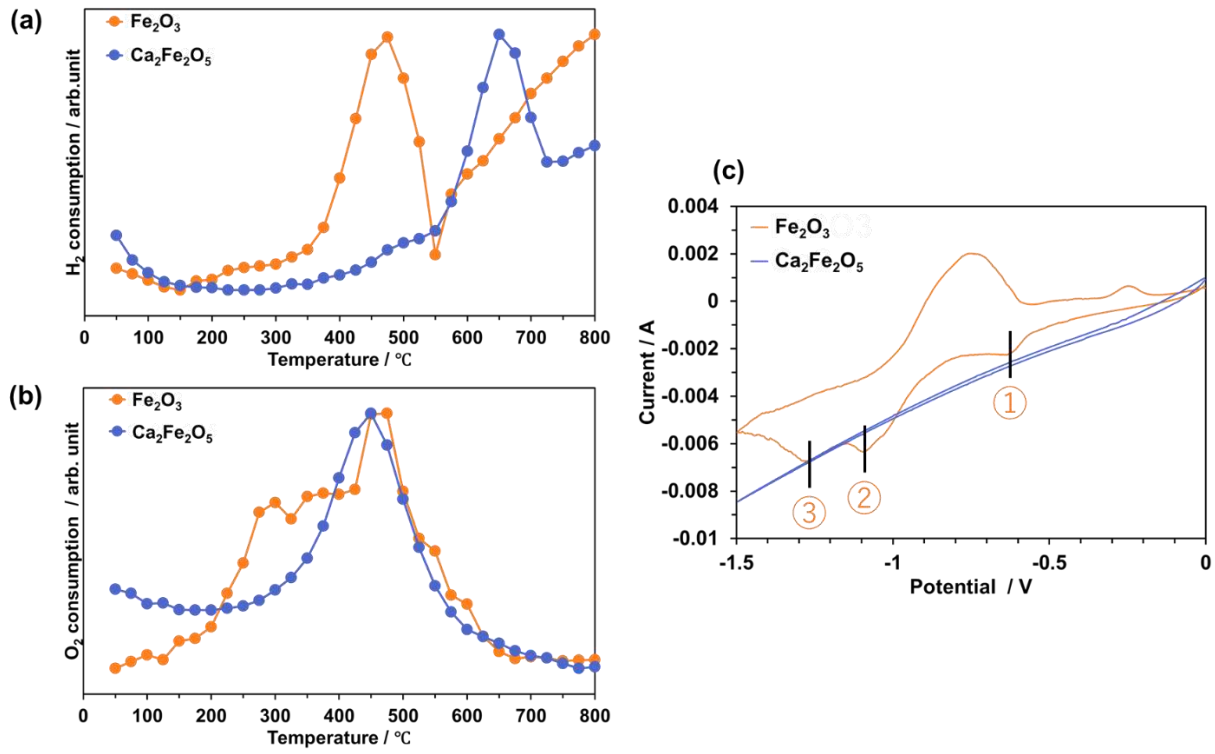

Figure 1. (a) H_2-TPR profiles and (b) O_2-TPO profiles for $Ca_2Fe_2O_5$ and Fe_2O_3 powders and (c) CV curves for $Ca_2Fe_2O_5$ and Fe_2O_3 electrodes. Gas mixtures containing 2% H_2 and 2% O_2 (He balance) were used for the TPR and TPO trials, respectively. The CV curves were recorded at 800 °C.

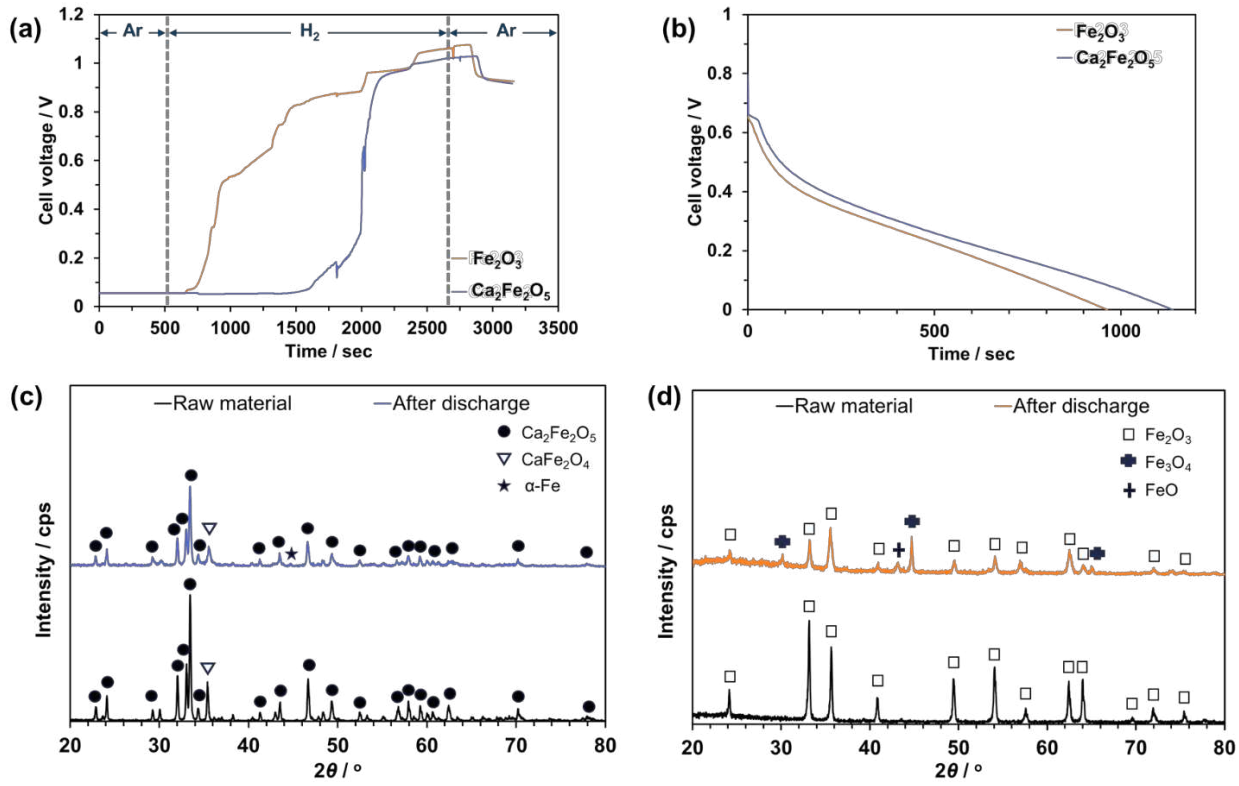

Figure 2. (a) OCV and (b) *V-time* plots for flow cells incorporating $Ca_2Fe_2O_5$ and Fe_2O_3 in the anode chamber and operating at 800 °C. XRD patterns obtained from (c) $Ca_2Fe_2O_5$ and (d) Fe_2O_3 residues after discharge. OCV data were acquired while switching from Ar to H_2 and back to Ar. After reduction with H_2, the *V-time* curves were recorded while supplying Ar.

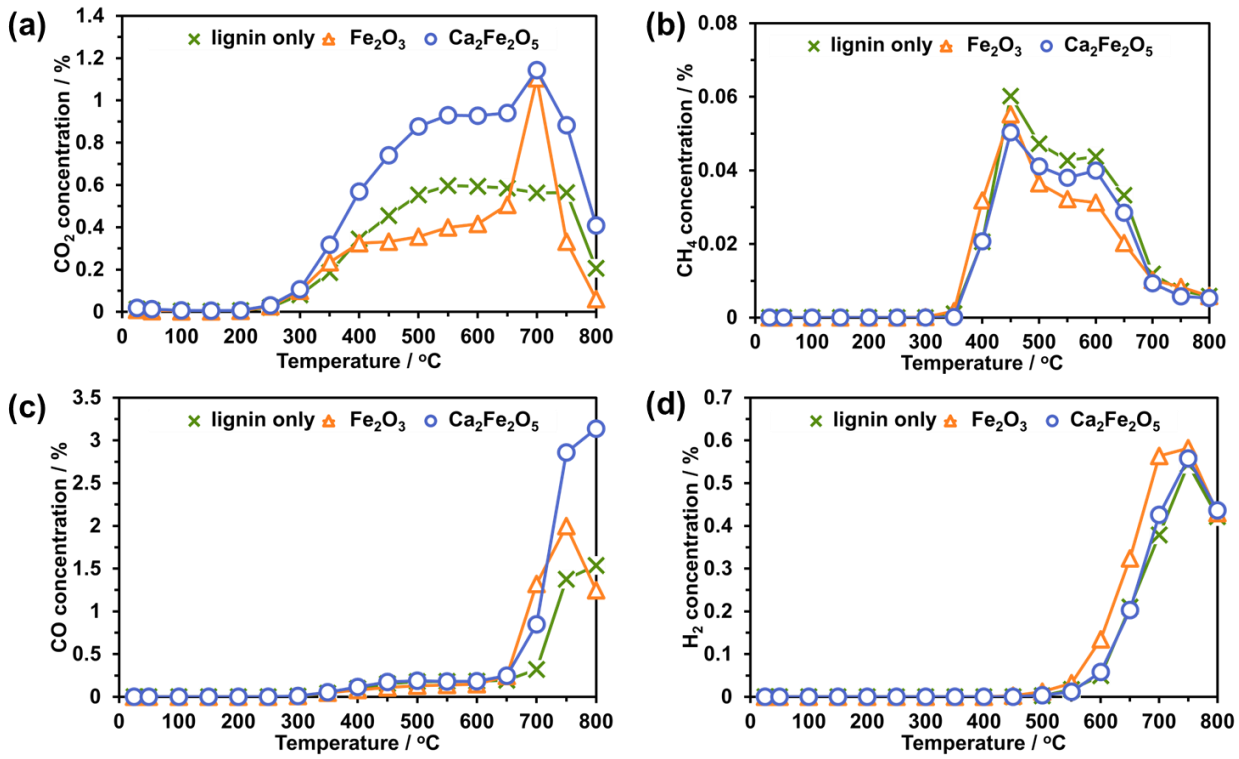

Figure 3. (a) CO_2, (b) CH_4, (c) CO and (d) H_2 concentrations in the outlet gases from mixtures of lignosulfonate and $Ca_2Fe_2O_5$ or Fe_2O_3 between room temperature and 800 °C. Data for lignosulfonate alone are also included for comparison. The mass of the lignosulfonate was fixed at 0.25 g with 0.126 mmol Fe in the two Fe-based compounds.

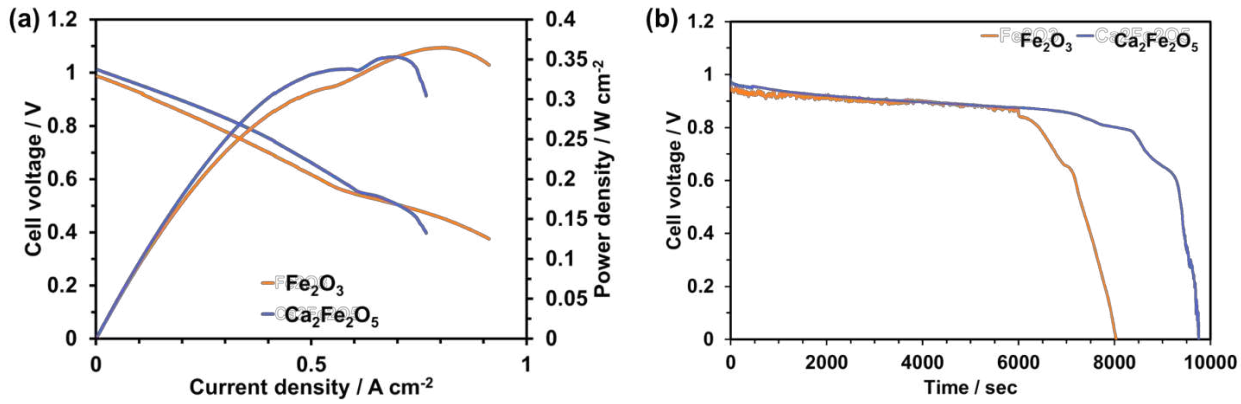

Figure 4. (a) *I–V* and *I–P* curves and (b) *V–time* curves acquired from $Ca_2Fe_2O_5$ and Fe_2O_3 cells at 800 °C. The masses of the lignosulfonate and of the two Fe-based compounds were the same as those provided in the caption to Figure 3.

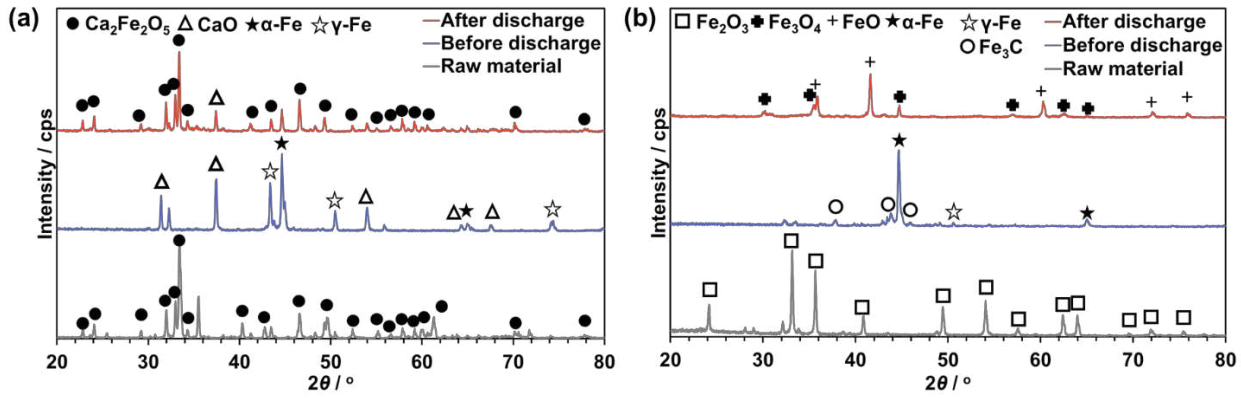

Figure 5. XRD patterns for (a) lignosulfonate/$Ca_2Fe_2O_5$ and (b) lignosulfonate/Fe_2O_3 mixtures before and after discharge at 800 °C and for the original raw materials. The masses of the lignosulfonate and of the two Fe-based compounds were the same as those provided in the caption to Figure 3.

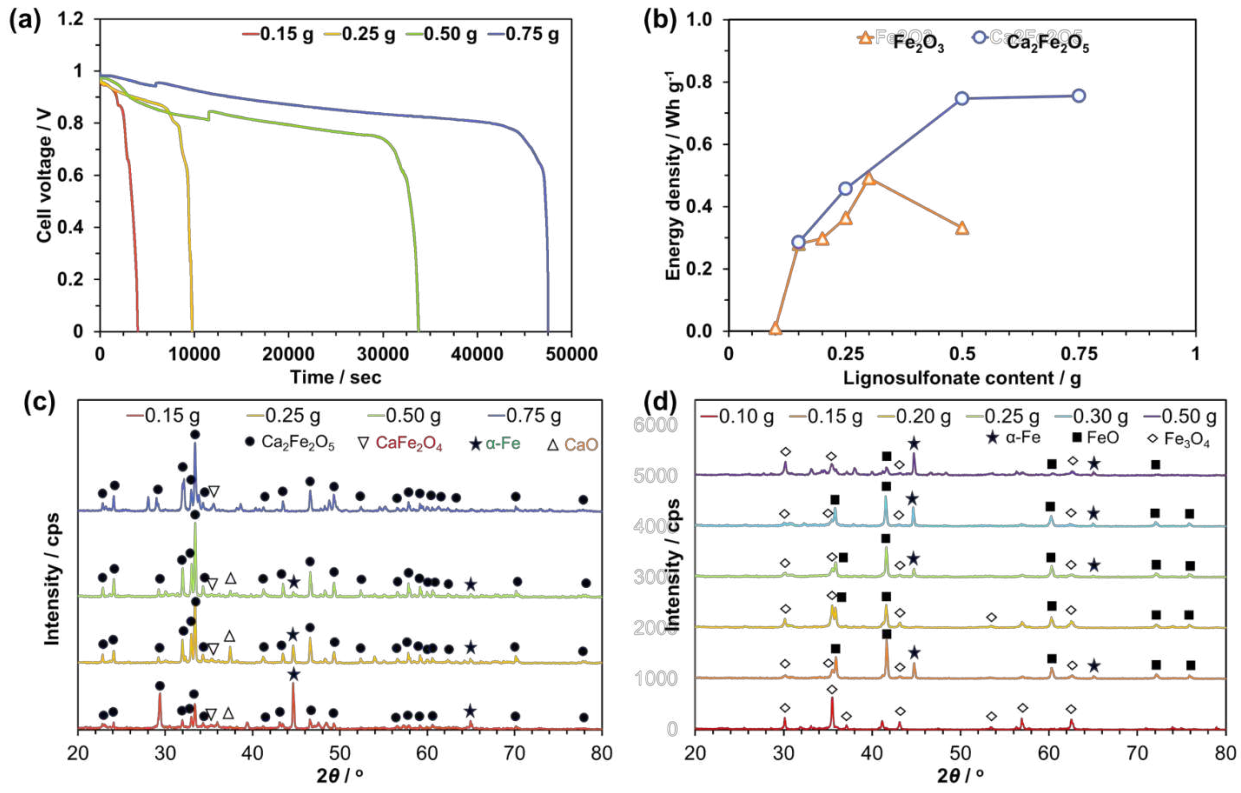

Figure 6. (a) *V–time* curves acquired using various masses of lignosulfonate at 800 °C, (b) energy density values as functions of the lignosulfonate mass, and XRD patterns for (c) lignosulfonate/$Ca_2Fe_2O_5$ and (d) lignosulfonate/Fe_2O_3 mixtures after discharge. Each of the two Fe-based compounds contained 0.126 mmol Fe.

Table of Contents

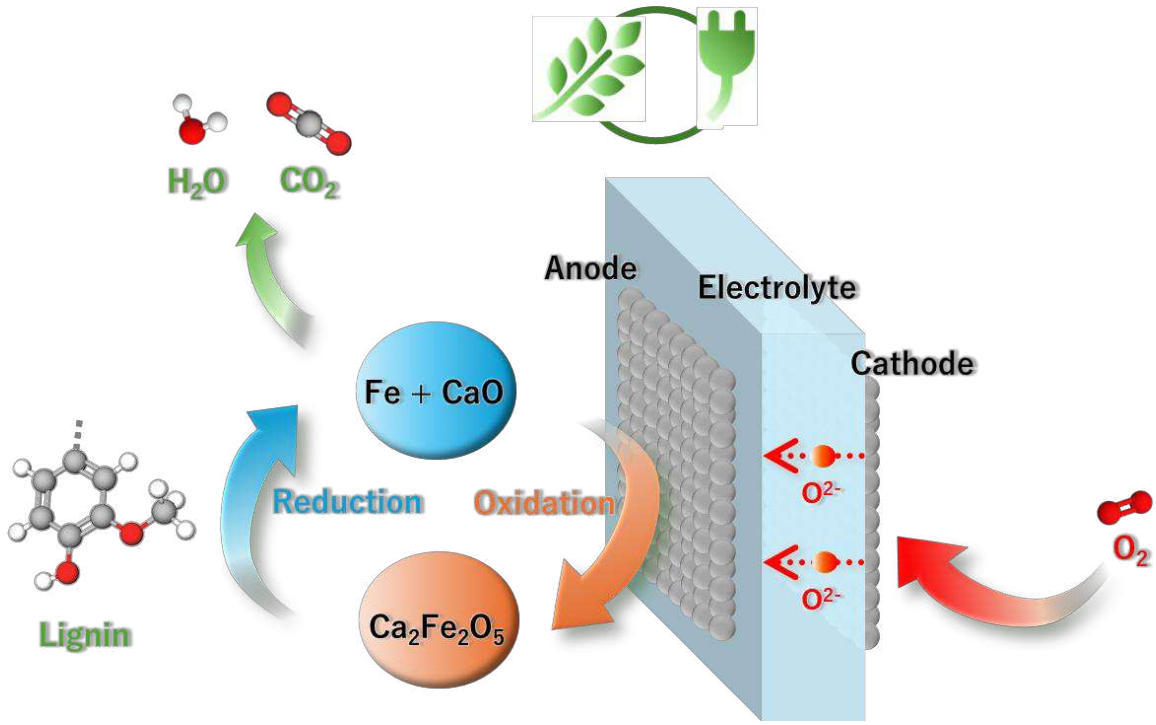

Supplementary Files

This is a list of supplementary files associated with this preprint. Click to download.

- Submittedsupportinginfomation.docx